Check for updates

Aerodynamic Behavior of a Biomimetic Wing in Soaring Flight – A Numerical Study

Eike Tangermann[1] · Gianantonio Ercolani[1] · Markus Klein[1]

Abstract

Multi-element wing tips based on bird wings appear attractive in soaring flight, where a minimal sink velocity is the design goal. The present study aims to reproduce the soaring flight observed from white storks (ciconia ciconia) in a biomimetic computational model in order to visualize and investigate the flow around and through the wing tip cascade. RANS and hybrid RANS–LES computations have been performed allowing access to all features of the flow field. The resulting properties in soaring flight have been compared to measured data of free flying birds from the literature to qualify the results of the re-engineered wing. Further, the flow field has been analyzed in detail to understand the underlying flow physics and to point out relevant phenomena such as a system of vortices associated with the wing and tip design which contributes to the observed aerodynamic properties.

1 Introduction

From many species of birds, wing tips can be seen on which the primary feathers are arranged in the shape of a cascade. Especially larger birds which spend a significant portion of their flight gliding or soaring show such multi-element wing tips. This comprises several birds from the order of birds of prey Accipitriformes (diurnal birds of prey) like eagles, vultures, ospreys or hawks but also Gruiformes (crane birds). Strigiformes (owls) have these cascades only to a smaller extent, whereas even some smaller birds which spend more time in flapping flight like those from the family of Corvidae (crow birds) as for example jackdaws show very pronounced feather cascades. Within the present work the

✉ Eike Tangermann
  eike.tangermann@unibw.de

  Gianantonio Ercolani
  g.ercolani@unibw.de

  Markus Klein
  markus.klein@unibw.de

[1] Department of Aerospace Engineering, University of the Bundeswehr Munich, Werner-Heisenberg-Weg 39, Neubiberg 85577, Germany

Springer

clade of Aequornithes (core water birds) is of particular interest from which not only the order of Pelecaniformes (e.g. pelicans, herons and ibises) but especially the Ciconiiformes (storks) feature wing tip cascades.

On the other hand it should be noted that the cascade is not the only tip shape occurring on larger birds. Pointed wing tips also appear in many bird species. Figure 1 indicates the shape of these two planforms. The order of Procellariiformes (tubenoses), to which petrels and the albatrosses belong, typically has clearly pointed wing tips with the feathers kept together. Those birds are famous for their gliding performance. However, they rather perform dynamic soaring and slope soaring, whereas the aforementioned birds, as far as they practice soaring, are focused on thermal soaring, where the challenge is even more about maintaining a sink rate as low as possible in order to gain altitude while keeping the airspeed reasonably low to allow for maneuvering inside the thermal column. This difference between pointed and cascaded wing tips, mostly between soaring birds on land and sea, was described by Graham (1932) in one of the first detailed investigations of cascaded wing tips on birds. Graham also proposed a drag reduction by the feathers arranged in a cascade.

Newman (1958), who has observed the flight of the black vulture, has highlighted that the aspect ratio and tip feather configuration is changed between soaring and gliding flight. In gliding flight at higher velocities elbow and wrist are bent to reduce the span, thereby achieving a lower aspect ratio. Concurrently, the tip feather slots are less exposed than in thermal soaring. This agrees with newer observations of white storks by Eder et al. (2015), who also provide quantitative descriptions of the wing aspect ratios. Newman further derives that multi-element wing tips only provide a reduction of induced drag if they are arranged in a non-planar configuration. Obviously, exactly this can be seen from observations of birds in flight.

A lot has been learned about birds in gliding flight from experiments in wind tunnels. Pennycuick et al. (1988) have performed measurements of aerodynamic performance on frozen waterfowls with a focus on the body drag, however. Shifting the focus towards the wing tips, (Tucker 1993) performed experiments on a wooden wing with the Clark Y airfoil featuring three different tip configurations, a single element tip and a three element cascade of Clark Y shape as well as one with three primary feathers of Harris's hawk. He was able to demonstrate a significant reduction of drag which was 12% less than other comparable wings. It is worth to note that the feathers, in contrast to the other tip configurations, have exhibited aeroelastic deformation by upward bending of the tips. Further, this bending motion also affects the local airfoil of the feathers. Eder et al. (2011) have shown an increase of camber while the feather is bending upward at higher load. Tucker continued his studies with measurements of a Harris's hawk gliding freely in a wind tunnel (Tucker 1995). He was able to demonstrate that the induced drag factor increased from 0.56 to 1.10 after clipping the wing tip feathers.

Fig. 1 Two major planforms can be seen for gliding birds, cascaded (left) and pointed (right) wing tips

Several other experiments have been performed with birds in wind tunnels mostly focusing on integral drag components and glide efficiency. The detailed flow around and through a feather casacade is difficult to access in wind tunnel conditions. Pascoe (2009) performed measurements on a mounted stork wing in a wind tunnel. Using particle image velocimetry (PIV) flow visualization of the wake flow, he observed how the cascade generates a tip vortex with multiple cores. A similar investigation has been performed by Klein-Heerenbrink et al. (2017) with a live jackdaw in gliding and flapping flight. The feather cascade shows beneficial behavior both in flapping and gliding flight. From the overall phylogenetic occurrence of cascaded wing tips it is concluded that this configuration originally has evolved for improvements in flapping flight. The conclusion also appears reasonable since in flapping flight as in thermal soaring the feather is operated at high lift, whereas in gliding flight the covered distance is the primary focus. This is further supported by the findings of Berens (2008) who, from numerical simulations of a wing with multi-winglet tips with the vortex lattice method, found out that the cascade is not significantly beneficial when targeting for maximal range. Instead, he could show a significant improvement for flight with maximal endurance which, like soaring, is performed at minimal sink rate.

Studies of birds in soaring flight are harder to realize as this cannot take place in a wind tunnel but only in free flight at significant altitude above ground level. Eder et al. (2015) have been using laser tracking devices to reconstruct the flight path of storks in soaring and in gliding flight. From this data, glide efficiency and speed polar curves for different phases of the flight were obtained. For soaring flight an induced drag factor of 0.81 indicates a significant effect of the feather cascade, which is fully open in this configuration. Inspired by these results, the present study aims for deeper understanding of the phenomena occurring around a stork's wing in soaring flight with focus on the primary feather cascade. Based on photographic images and numerical flow simulations with the vortex lattice method, the geometry of a stork wing has been re-engineered and then applied to Navier-Stokes flow simulation. Reynolds-averaged Navier-Stokes (RANS) simulations have been performed to cover a large range of the angle of attack together with scale-resolving simulation at a selected condition for detailed insight to the turbulent flow. Since Large-Eddy simulation (LES) requires too much computational effort in the present case, the scale-resolving approach is of hybrid RANS-LES type. Performance results have been compared and validated for plausibility with measurement data by Eder et al. (2015) from live white storks.

2 Setup and Modeling

2.1 Geometry and Reference Quantities

The present study is focused primarily on the wing and its tip region. Therefore, the stork's torso has not been considered in the Navier-Stokes flow simulations. Despite its contribution to overall lift and drag, it is not involved in the flow patterns around the wing tip. Nevertheless, for the comparisons of aerodynamic performance an estimated value for the body drag has been considered. Figure 2 shows the geometry featuring one side of the wing and bounded by a symmetry plane in the middle plane of the bird. On the wing tip a cascade of nine primary feathers is attached. As a simplification compared to the example from nature, all geometry is non-permeable and has a smooth surface.

Following representative average data of white storks, the half wing span of the model has been set to $b = 1.02\,m$ resulting in a reference surface of $A_{ref} = 0.3018\,\mathrm{m}^2$ for the half

Fig. 2 Wing geometry with cascade of primary feathers
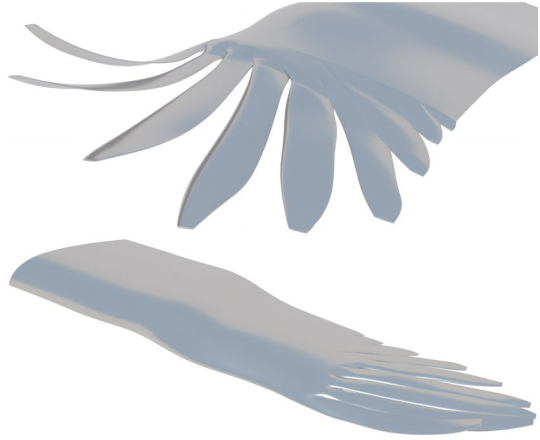
model. To determine the absolute sink rate, a mass needs to be specified for the bird, which is $m = 3.5\,\text{kg}$ and the value of the air density is considered to be $\rho = 1.225\,\text{kg/m}^3$ based on standard atmosphere at sea level. These dimensional quantities allow for a comparison with data from the referenced experiment (Eder et al. 2015), which are based on similar conditions. However, the relative trend along the drag and speed polars remains the same independent of the reference quantities. Finally, the Reynolds number of the wing based on average chord length is $Re = 230000$. From this relatively low Reynolds number it can be expected that laminar boundary layers and transition with and without flow separation will appear in the flow field.

The initial design of the wing is based on photographic images of birds in flight. The wing airfoil sections at shoulder, elbow and wrist location are taken from descriptions by Herzog (1968) and blended in an appropriate way. The resulting sections at three different locations are shown in Fig. 3. At its tip, nine primary feathers are attached, of which the aft three ones can be considered as one element. Figure 4 shows their arrangement and labeling of the feathers. The feathers act like a multi-element airfoil. The flow around and between them features a strong interdependence among the primaries in down- and also upstream direction. In order to design and arrange them, computations with the vortex
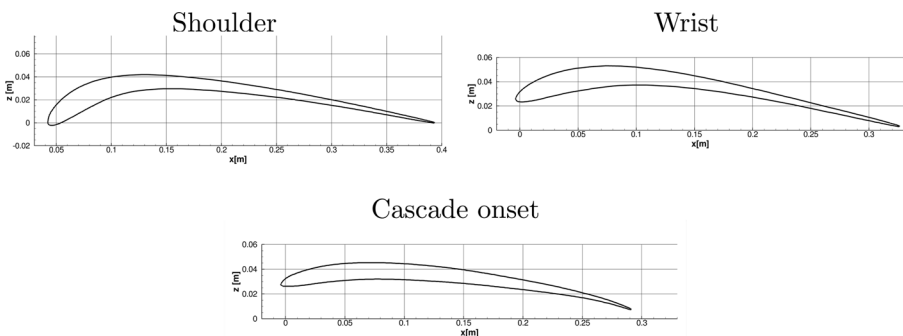

Fig. 3 Airfoils sections of the wing at shoulder (symmetry plane), wrist ($y = \pm 0.5m$) and onset of the cascade ($y = \pm 0.69m$)
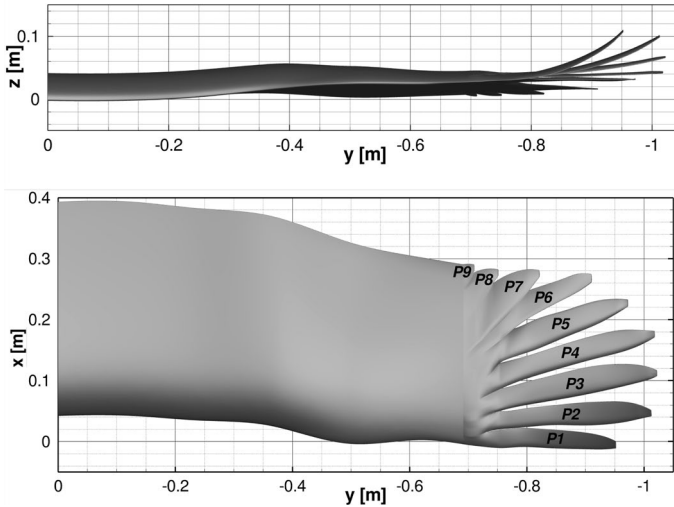
Fig. 4 Views to the geometry from front and from top. The individual primaries are labeled P1–P9

lattice solver FLZ_Vortex, version 1.217 (FLZ 2022) have been performed with an iterative process towards the best performance in terms of minimal sink rate. Even though the vortex lattice method appears as a lower-fidelity approach compared to Navier-Stokes simulations, it is a valuable tool in the preliminary design stage. It allows to determine aerodynamic parameters of the wing configuration in an extremely efficient way in terms of computational effort. In the present context, it is the only method which allows for a systematic variation of the parameters for all individual primary feathers. The model consists of 2656 surface panels and also features an indicated body of the bird. Figure 5 shows the panel model. It needs to be noted that only seven primary feathers appear here as the rearmost two feathers are considered being part of the outer end of the wing. Actually, the main wing of the panel model extends to the span-wise location where the feathers split up, whereas for the Navier-Stokes model from computer aided design (CAD) the primary feather surface elements already start at a location further inboard where the outermost

Fig. 5 Panel model of the wing for vortex lattice method for optimization of the feather cascade
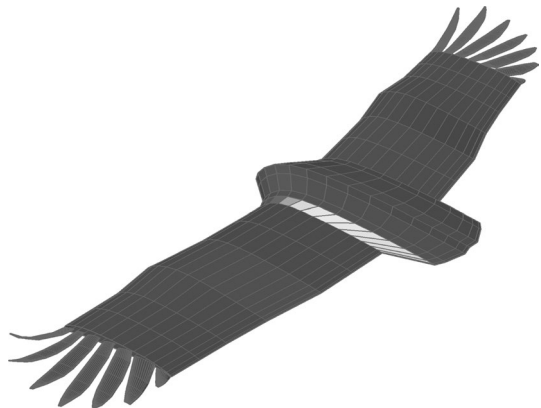
airfoil is prescribed and the surfaces start blending into the individual feathers. It is not necessary to consider this shape blending in the vortex-lattice calculations. Figure 6 shows sections through the feather cascade at six different span-wise locations. The front feathers feature a negative inclination to compensate for the upward movement of the flow induced by the following elements similar to a typical wing slat.

The torso indicated in the figure has only been used in this part of the study while arranging the tip feathers. For the performance analysis from Navier-Stokes data, the value of the drag coefficient for the torso plus interference drag has been estimated to be $C_{d,torso} = 0.0077$ with the same reference quantities as for the wing drag. The estimation is based on vortex lattice calculations assuming a streamlined body. In all performance plots, this value has been added to the drag calculated for the plain wing.

2.2 Computational Modeling

To cover a large range of the angle of attack, steady RANS simulations have been performed using Ansys Fluent, Release 19.1. Since the Mach number is nearly zero and no compressibility effects need to be expected, the formulation of the steady Navier-Stokes equations is incompressible with SIMPLEC pressure coupling. The flow field features significant laminar regions including laminar flow separation as well as transition to turbulence. Therefore, the shear stress transport (SST) turbulence model by Menter (1994) together with the γ-Re_θ transition model from Langtry and Menter (2009) has been selected. Curvature corrections according to Smirnov and Menter (2009) have been applied for improvements in the prediction of tip vortices. Spatial discretization has been chosen as second order accurate upwind for the convective terms in all transport equations.

For a selected case with angle of attack $\alpha = 7°$, which is within the range of best sink rate found from RANS, a hybrid RANS-LES computation has been performed. The Open-FOAM flow solver toolbox version 1812 (Weller et al. 1998) has been used in this case since a turbulence model specifically suitable for the present low Reynolds number flow conditions was already available and validated from previous work (Tangermann and Klein 2021). The hybrid model is the SST-based delayed detached eddy simulation (DDES) model according to Spalart et al. (2006), which has been supplemented with a transition detection following the same model by Langtry and Menter as in the RANS case. This is required in order to suppresses the turbulence model from being active in laminar boundary layers. Otherwise it would not be capable of predicting laminar separation since eddy
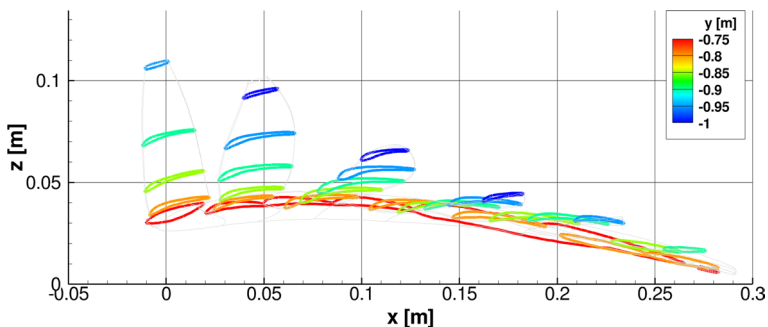

Fig. 6 Sections through the primary feather cascade colored by span-wise coordinate y

Fig. 7 Numerical mesh for the RANS case. Entire wing (top), leading edge at symmetry plane (middle) and tip of second primary feather (bottom)
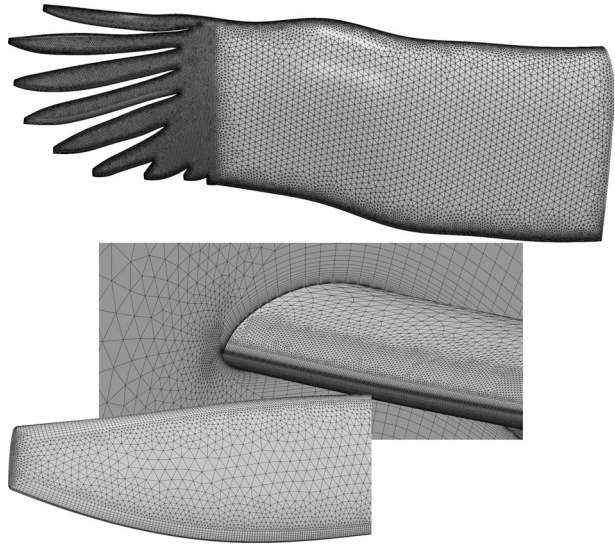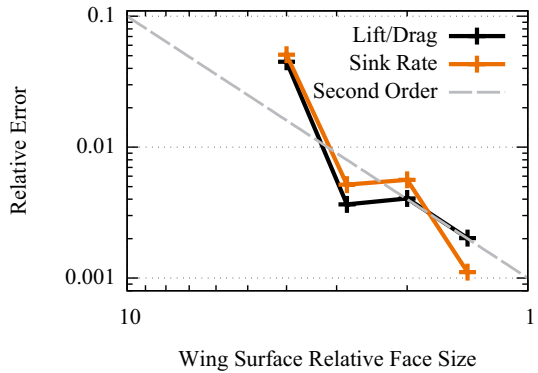

Fig. 8 Results from mesh convergence study, relative error of glide efficiency and sink rate compared to the finest mesh over surface cell size normalized by finest mesh cell size

viscosity would immediately lead to formation of a modeled turbulent boundary layer velocity profile. Like in the RANS setup, the Navier-Stokes equations have been treated in an incompressible but now time-resolving formulation. The temporal discretization is a second order accurate backward scheme. Spacial discretization also is second order accurate using a central scheme blended with 25% upwind for stabilization.

The computational domain is bounded by a hemispherical farfield which is located at a distance of 50 times the half-span around the wing. Figure 7 shows the mesh for the RANS case. It is an unstructured mesh based on tetrahedra with prism layers around the surface. Edges with smaller radii have been resolved using quadrilateral faces. The primary feathers are resolved finer than the main wing to allow for capturing more details of the flow through the cascade. For a full resolution of the boundary layers on the wing surface, the first cell layer has a non-dimensional thickness of $y^+ \leq 1$. As result from a convergence study, the mesh features a total number of 9.35 million cells. Figure 8 shows the convergence of the refinement process. Five different meshes have been compared with a reduction factor of $1/\sqrt{2}$ in each step concerning the cell size on the main wing and primary

feather surfaces. The plot shows the deviation of resulting glide efficiency and sink rate relative to the results of the finest mesh. With the deviation approaching 0.1%, the refinement has been stopped.

The DDES mesh follows a very similar structure as the RANS mesh but features significantly finer cells. Based on estimates for the turbulence length scale from RANS in order to cover the expected turbulent structures, it features a total of 47.5 million cells.

3 Results

The RANS simulations cover a range of $\alpha = -8°$ to $\alpha = 14°$ for the angle of attack reaching from below zero lift up to full stall. In Figure 9 all computed cases are indicated with gray crosses. Two ranges are resolved very fine. They reach around the states of best glide efficiency ($\alpha = 3° - 5°$) and lowest sink rate ($\alpha = 6° - 8°$) in order to offer a detailed view to these most relevant ranges in which most of the flying is expected. However, for best glide the actual stork would shift the wings to a slightly lower aspect ratio and re-arrange the primary feathers as described by Eder et al. (2015). Therefore, this case is less relevant in the present observations and mostly reviewed for the sake of completeness. The curve in Figure 9 shows the best glide ratio of $C_l/C_d = 12.132$ at $\alpha = 4.6°$. Eder et al. (2015) even report a maximum value of $C_l/C_d = 15$ from their measurements of free flying storks.

To provide another perspective to the glide efficiency, Figure 10 shows the drag polar over the entire investigated range. The best glide at $\alpha = 4.6°$ is also indicated by a tangential line. The minimal drag does not appear for zero lift conditions. This happens due to the severely non-planar configuration and geometric as well as aerodynamic twist of the wing. Zero lift is achieved at approximately $\alpha = -4°$ whereas the minimal drag occurs at $\alpha = -1°$.

Due to its computational effort, the DDES is limited to one angle of attack. It has been performed at the best sink rate condition of the plain wing configuration (without

Fig. 9 Glide ratio over angle of attack. The gray crosses indicate the cases computed with RANS. The DDES average value is supplemented by bars to indicate the range of 67% confidence from temporal fluctuation
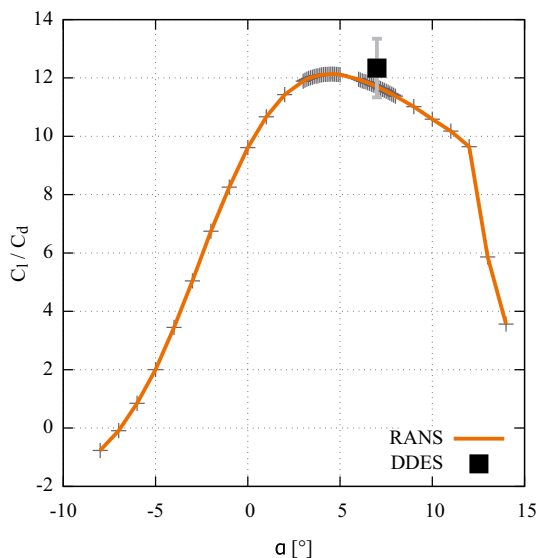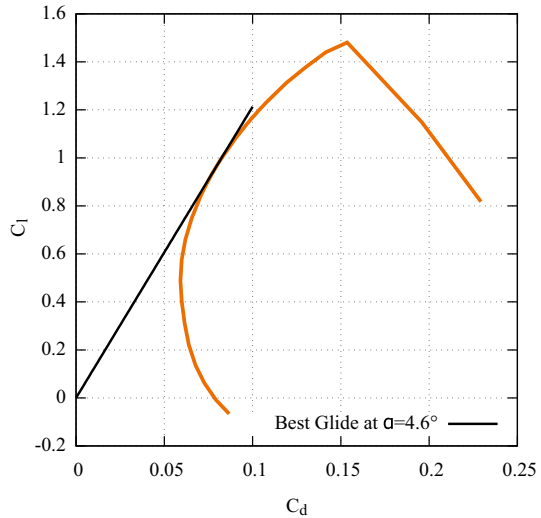
Fig. 10 Drag polar with indication of best glide angle at $\alpha = 4.6°$

considering torso drag) which is achieved at $\alpha = 7°$. As will be shown below, the sink rate remains relatively low along a wide range of angles of attack. Even though the wing and body configuration achieves the optimal sink rate at $\alpha = 7.8°$, the former condition still offers a very efficient setting. The DDES predicts a slightly better mean glide efficiency than the RANS at this state, for which the reasons will be discussed below. Further, the DDES also shows strong variations with time due to changes in the regions of separated flow. This impact is indicated in the plots by showing bars with the range of 67% confidence from all recorded samples.

Figure 11 showing the sink rate over angle of attack gives an impression of the operational range, in which good sink performance can be achieved. It is notable that even though a clear minimum determined from RANS computations occurs for $\alpha = 7.8°$, a wide

Fig. 11 Sink rate over angle of attack. The gray crosses indicate the cases computed with RANS. The DDES average value is supplemented by bars to indicate the range of 67% confidence from temporal fluctuation. The best sink rate according to Eder et al. (2015) is indicated by the dashed line
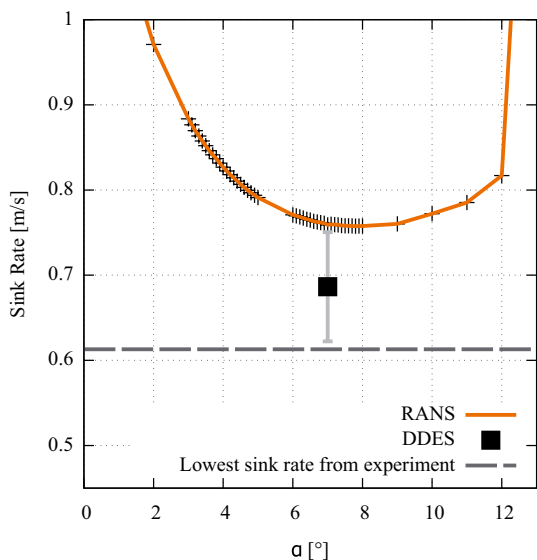
range of α offers low sink rates. Obviously, the design allows a good amount of flexibility and tolerance to choose the angle of attack during soaring without too much sensitivity for the resulting sink speed. The optimal sink speed from the RANS computations at $\alpha = 7.8°$ results in $V_s = 0.7575\, m/s$ but all values between $7° \leq \alpha \leq 8°$ are below $V_s < 0.76\, m/s$.

As it might have been expected from the results for glide efficiency, the DDES predicts an even slightly lower sink rate of $V_s = 0.6864\, m/s$ as average value. As mentioned above, the DDES predicts significant variations in time. In Fig. 11 the range of 67% confidence for all samples is again indicated by bars. It ranges more than $\pm 0.05\, m/s$ around the mean nearly reaching both the RANS value as well as the best value found from regression of the measurements by Eder et al. (2015), which is approximately $V_s = 0.613\, m/s$.

To come to a comparison with the measurements along a wider range of flight conditions, Fig. 12 provides the speed polar plot. The black line is a regression curve from the measurements by Eder et al. of storks only in soaring wing configuration. The measured data points for airspeed versus sink rate have been split into three divisions related with the three different flight stages of soaring, efficient gliding and high speed flight. For each of these data groups regression curves have been presented in the original paper based on a functional expression. It takes the form

$$V_S = m_1/V + m_2 V^3 \tag{1}$$

with the coefficients m_1 and m_2 providing a physical representation but being achieved from data regression and the airspeed V. Its derivation and interpretation can be found in the original publication. From these three regression curves, the parameters for soaring are shown in Fig. 12. The RANS results show a qualitative agreement with the regression function but generally predict a higher sink rate. The DDES comes even closer with the range of fluctuations again reaching between the measurement and RANS results.

There are several factors to explain why some deviation from the measured data occurs. The geometry based on photographs, bird wing sections from the literature and vortex lattice optimization provides some uncertainty, which is hard to quantify. However, the present results indicate that it comes very close to the actual geometry. Beyond the geometry,

Fig. 12 Speed polar of the wing. The DDES average value is supplemented by bars to indicate the range of 67% confidence from temporal fluctuation. The black line provides a regression curve by Eder et al. (2015) from their measurements for the soaring configuration
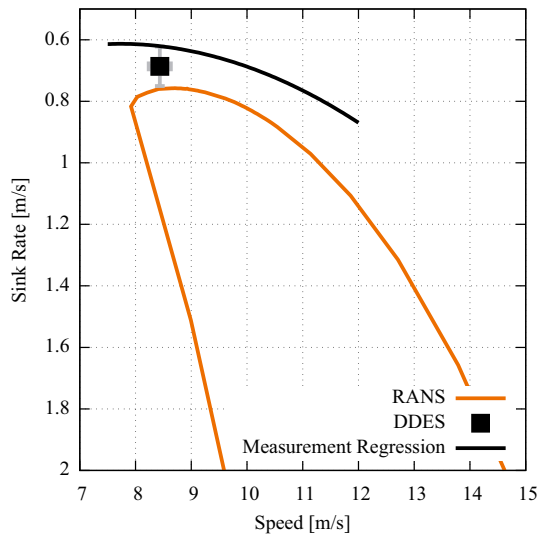
the real life stork has a lot more features, which have not been considered in the present study. The feathers have a non-smooth surface, which supposedly has an impact on the near-wall turbulence behavior and thereby on the flow separation. Also, the trailing edge of the wing is not a straight line as in the present model. Instead it has a wavy shape formed by individual feathers. Further, the primary feathers are air-permeable as demonstrated by Eder et al. (2011). This significantly changes the flow separation behavior on the primaries. Elasticity of the primary feathers might also be an important factor as the elastic feathers are known to undergo strong bending deformations during flight. Presumably this behavior has been accounted for by the geometry design coming close to the geometry of a flying stork. However, the stork also might actively achieve some flow control by minimal movements in order to continuously maintain flow conditions in an optimal way.

Using the same procedure as performed in reference (Eder et al. 2015), the induced drag factor k can be determined from the coefficient m_1 in Eq. 1. k represents the ratio between the induced drag of the present wing and that of a planar wing with ideal elliptic lift distribution. Following the reference, Eq. 1 has been fit to the computed sink speed from the simulations within the range of $\alpha = 4° – 12°$ corresponding approximately to $V = 8\,m/s$ to $12\,m/s$. The fitted function exhibits a mean deviation of 1.6% from the computed sink rate, which is considered acceptable in this case compared to the uncertainties of the setup. This yields a value of $k = 0.899$, indicating that the present wing configuration features an induced drag 10% lower than a comparable planar, elliptic wing. Eder et al. even conclude a value of $k = 0.81$, which again indicates that the real stork performs better than the present model.

As mentioned above, the DDES predicts fluctuations of the aerodynamic properties over time. The temporal variations of glide efficiency as well as sink rate in theoretical equilibrium gliding are shown in Figs. 13 and 14, respectively. These variations are mostly attributed to changes of separated patches on the inner wing surface coming from fluctuating laminar separation and consequent re-attachment. In the interpretation of these plots, it needs to be considered that they represent ideal equilibrium glide conditions, where changes of glide efficiency immediately translate into changes of airspeed and sink rate

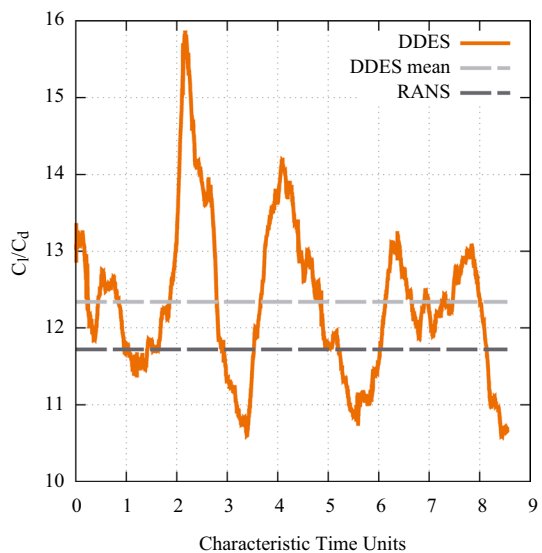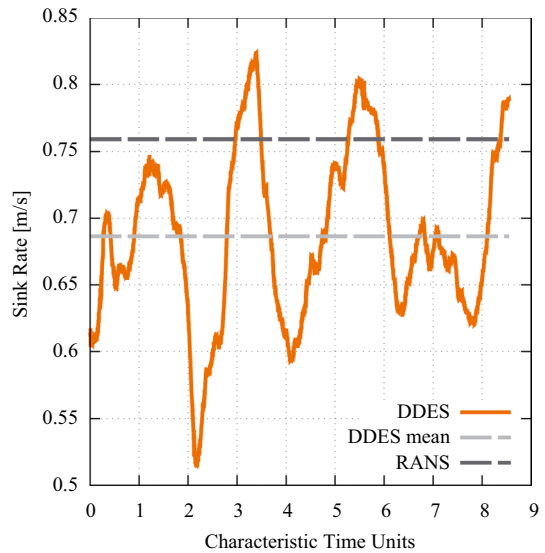**Fig. 13** Variation of glide ratio over time predicted by DDES for $\alpha = 7°$

Fig. 14 Variation of sink rate in equilibrium gliding flight over time as predicted by DDES for $\alpha = 7°$

neglecting inertial damping. The characteristic time unit is the time which it takes the freestream flow to pass the wing chord depth. The plots of variation in time are not long enough to confirm a true periodic behavior. However, the curves provide such an indication. Assuming that four cycles appear in the curves, the resulting Strouhal number is $Sr = 0.054$ based on freestream velocity and reference chord depth. In dimensional units for an average stork flying at the conditions predicted by the DDES, this means a frequency of approximately 12.5 Hz, during which the bird would encounter a variation of lifting force by $\pm 10\%$ of its own body weight at most. Due to its inertia, the flight path would certainly not encounter the theoretically computed changes in sink rate. However, it appears like a rather rough and uncomfortable flight for the bird.

It is assumed unlikely that a real bird would encounter variations of its wing aerodynamics as described here. However, most simplifications and neglects with respect to real feathers and wings have an impact on near-wall flow, and thereby in particular on flow separation. Thus, it can be assumed that the fluctuations are mostly caused by the model simplifications.

A closer look to the flow field is provided by Figs. 15 , 16 17 for the conditions of $\alpha = 7°$. The footprint of the flow along the upper side wing surface is shown by surface streamlines from wall shear in Fig. 15 from both RANS and DDES, where the DDES view with streamlines represents the mean flow field. They are shown together with regions of separated flow, which for DDES are additionally shown from an instantaneous snapshot. The most significant difference between both approaches is the extension of those separated flow zones. RANS predicts an almost straight separation line along the entire main wing. This is a typical laminar separation forming a thin separation bubble above which the transition to turbulent flow occurs. Once the shear layer instabilities have broken up into turbulence, the flow re-attaches forming a turbulent boundary layer. The phenomenon of laminar separation does not necessarily lead to a wing stall as lift still is produced and the flow can re-attach. In DDES this is predicted in a similar way but in the mean flow field only in the inner third of the wing span such a separation bubble appears. Actually, in the instantaneous flow field the onset of the separation is corrugated. Here the flow also

Fig. 15 Surface flow field for $\alpha = 7°$ from RANS and mean DDES and instantaneous DDES. Streamlines from wall shear stress, surface coloring from pressure coefficient. Orange zones indicate separated flow
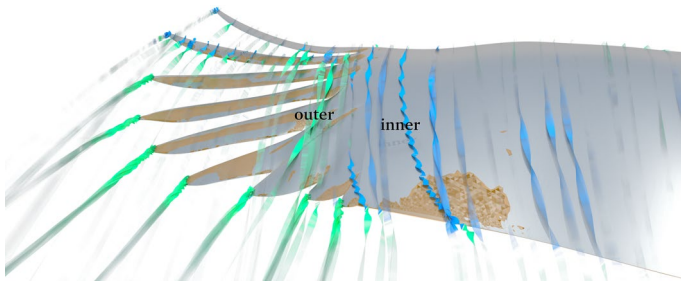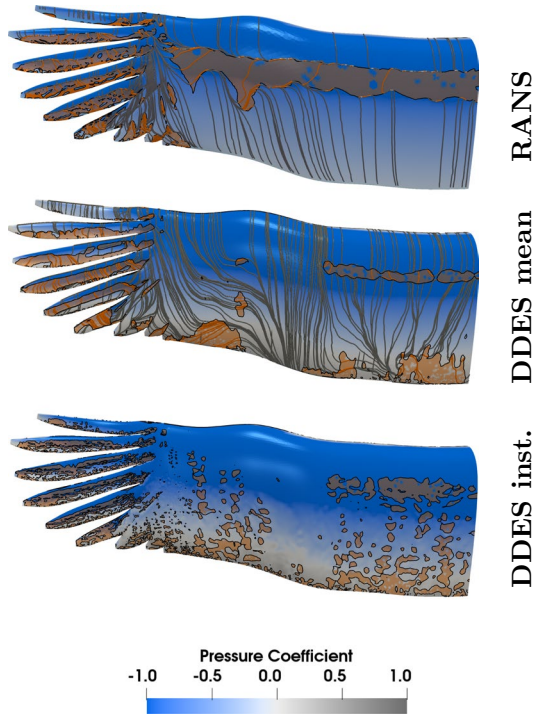

Fig. 16 Flow streamlines for $\alpha = 7°$ above the outer wing from mean DDES. Blue streamlines indicate counter-clockwise and green clockwise vortex motion. Orange surfaces mark flow separation

undergoes transition. After the first zone of separation, only isolated spots of separated flow appear which are traveling along the surface with the flow. Typical for laminar separation, these spots are smoothed out by attached flow regions in the mean field leading to the false impression of fully attached flow when only regarding the mean field. Towards the trailing edge, the flow tends to separate again, hence separated zones appear again in the mean flow field. In the outer part of the main wing no primary zone of separation appears. Instead, only spots of separation are visible in the instantaneous view. Above these spots the same transition mechanism generates fluctuations which, by extending laterally, form a turbulent boundary layer. Towards the trailing edge a stronger separation zone also appears
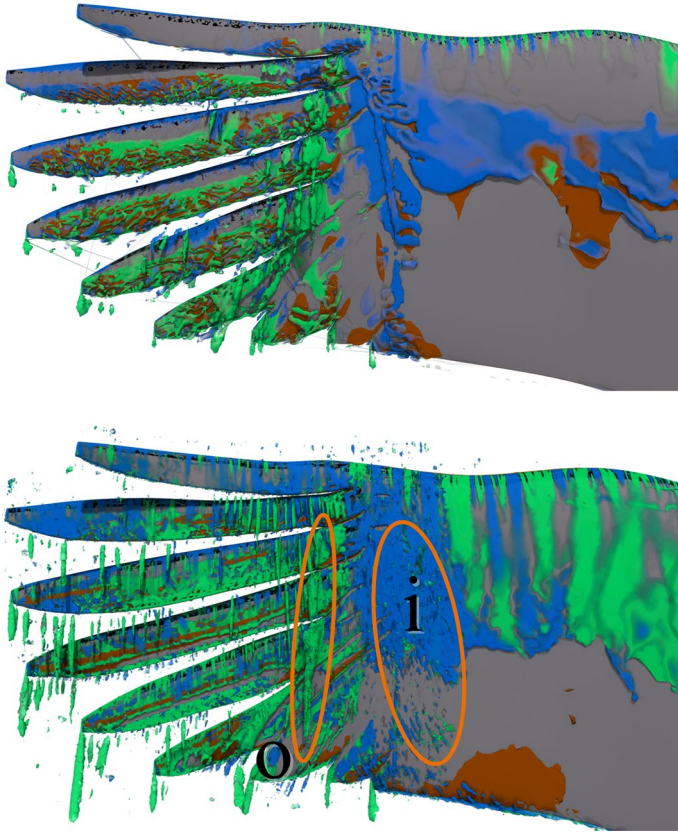
Fig. 17 Isosurfaces from Q-criterion for $\alpha = 7°$ from RANS (top) and DDES (bottom) colored by helicity. Blue and green indicate vortex orientation as in Fig. 16. Orange surfaces mark flow separation

in this outer part of the wing. These differences between RANS and DDES explain the deviation in the aerodynamic predictions between the results from both.

The flow across the primary feather cascade does not show such significant differences. All primary feathers show flow separation. In all cases this is laminar separation and does not lead to an airfoil stall. The first to third feather are inclined slightly negative and thereby also show a separation on parts of the lower side. However, due to the interference between the feathers they still provide positive lift. The foremost primaries even contribute a forward pointing net force as will be discussed below.

A system of several vortices dominates the flow structure through the cascade and also the outer part of the main wing. The surface streamlines in Fig. 15 already indicate the presence of vortices by pointing inbound towards the body, which is in particular visible from the DDES flow field. Figure 16 shows streamlines in the fluid above the surface for the outer part of the wing. The streamlines indicate different orientation of the vortical motion. The most intense vortices appear from the feather tips like small conventional single-element wing tip vortices. The first two primaries feature weak counter-clockwise rotating tip vortices indicating that the pressure difference is
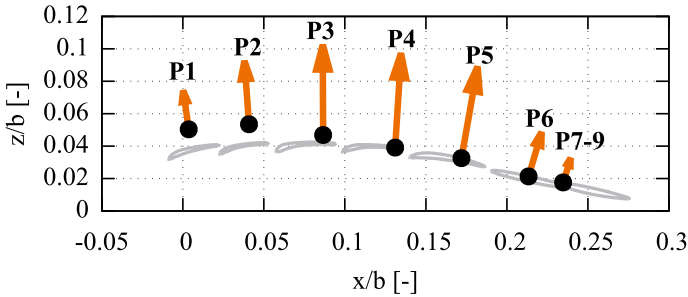
Fig. 18 Lift and drag vectors by the individual primary feathers (orange arrows), with the base point (black circle) located at the geometric center of each feather. Indication of airfoil section at $y/b = 0.8$ (not identical with geometric center)

reversed in the tip region. However, they still provide an overall lift as also will be discussed below. The other primaries show typical lift-induced tip vortices with clockwise rotation.

Besides these obvious tip vortices two other vortex regions appear in context with the feather cascade. The inner one, which is labeled in Fig. 16, is very pronounced and obvious in the streamline plot even though it is the weaker one. It is rotating counter-clockwise and towards the trailing edge it bends inbound. Thereby it induces a trailing edge separation region.

This inner vortex can be interpreted as a counter-rotating secondary vortex to the outer vortex, also labeled in the plot. In the volume streamlines, its origin can be seen as it evolves between the first three primary feathers, whereas in the surface streamline plot it causes an outbound motion on the trailing cascade feathers. The plot of Q isosurfaces in Fig. 17 gives another impression of this vortex. It results from the flow from the lower side passing between the primary feathers and it can be considered as the tip vortex of the main wing. However, by passing between the primaries, where the fluid even gets accelerated, the flow induces lower pressure on the feather upper side and thereby additional lift. The vortex which then is formed does, however, not induce significant lower surface pressure on the upper side of the outer main wing.

The surface flow pattern in Fig. 15 has shown only minor differences between RANS and DDES for the flow along the primary feathers. Fig. 17 shows considerably stronger differences in this region. Qualitatively the distribution of vortices rotating clockwise and counter-clockwise is very similar. But the strength of the vortices is predicted differently. Due to the coarser grid resolution in combination with increased viscous damping of the RANS model, the vortical structures from feather tips as well as those further inwards appear weaker despite the rotational correction term being applied. Nevertheless, since these vortices do not interact with downstream surfaces and do not show a direct impact on the surface pressure, the resulting aerodynamic predictions are rather similar.

Within the primary feathers in the wing tip cascade and also with the main wing a strong interaction occurs. The flow is affected by each surface and the local angle of attack especially for the tip feathers differs strongly from the freestream value. These flow deflections have been the driving force in the design of the cascade and prescribe the local angle of incidence. It is a complex system featuring many mutually interacting parameters. The first three primaries are inclined slightly negative relative to the wing as an adaptation to

the flow deflection where they are situated in an upwash flow. As mentioned above, these feathers show a counter-rotating tip vortex, which means that towards the tip the pressure difference between lower and upper side vanishes. As the upwash from the main wing decays towards the tip, the outer part of these feathers experiences flow under a lower angle of attack. The net contribution to the force still is positive lift as indicated in Fig. 18 which shows contribution to lift and drag from all primaries at an angle of attack of $\alpha = 7°$. The indicated feather sections originate from the location $y/b = 0.8$ which is close to the inner end of the cascade. Further towards the tip the slots between the feathers become greater.

Due to their negative inclination, the three front feathers even produce a negative drag force, pointing forward. For the first two feathers it is very obvious, the third feather has slightly negative drag which is almost zero. Considering all primary feathers, the lift distribution looks very similar to a single element airfoil as could have been expected. The contribution of the rearmost three feathers is quite low not only because of its smaller surface but also because the pressure difference between lower and upper side is decreasing towards the trailing edge.

Figure 19 shows slices through the feather cascade normal to the span to illustrate the flow between the primaries at $\alpha = 7.8°$ with lowest sink rate. The contour color indicates the span-wise velocity component. Since it is the left wing at negative y coordinate, positive velocity is pointing inbound towards the body. The streamlines represent in-plane velocity not considering the span-wise component. They are colored by velocity magnitude indicating how the flow is accelerated above the section and especially in the slots between the feathers. From this perspective, the cascade appears like a multi-element airfoil in high-lift configuration. Especially at $y = -0.8$ m and -0.85 m but also in the other sections the acceleration between the feathers is obvious, which then induces lower pressure on the upper side of the following feather. This effect is mostly unaffected by the span-wise velocity, which is close to zero in the slots.

According to the overall pressure differential, the flow is pointing outbound on the lower side and inbound on the upper side forming the typical tip vortex structure. On the lower side, the area of highest outbound velocity is located in the rear part and especially in the outer sections of feathers four and five. The inbound movement on the upper side is shifted above the feathers by the flow through the slots. From $y = -0.8$ to -0.95 the region of low span-wise velocity becomes thicker as the slots become wider. In the outermost slice, close to the tip, each of the feathers features its own vortex due to increased spacing. Spots of outbound pointing velocity appear on the upper side of some feathers near their trailing edges. They are connected with local separation and fed from the lower side. On the other hand, the first to primaries show inbound velocity in the outer sections close to their leading edges. This results from their upward bent shape which induces an inbound component to the velocity field. Figure 19 reveals a strong interdependence among the primaries concerning spacing and inclination and underlines that their arrangement is a highly multidimensional process. In the present configuration they serve as a multi-element wing fed by the tip vortex of the inner wing while reducing their own tip vortex impact by appropriate shaping and spatial separation of the individual tip vortices.
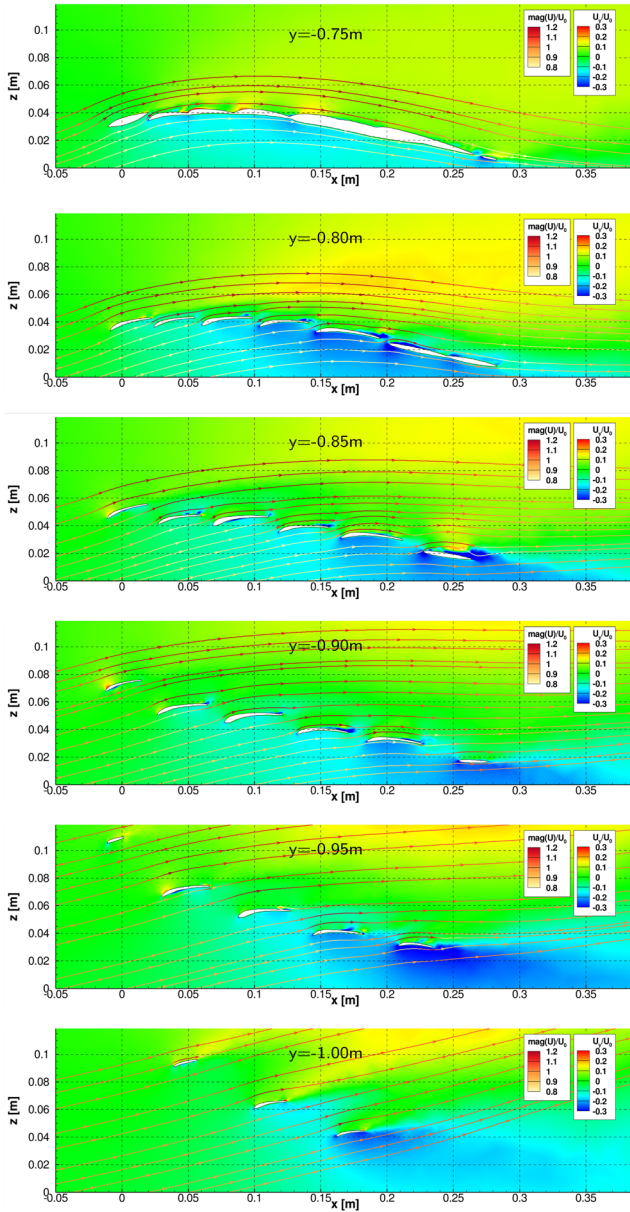
Fig. 19 Flow field around and between the primary feathers on the left wing tip (negative *y*) for lowest sink rate ($\alpha = 7.8°$) from RANS. Contours colored by span-wise velocity component (positive pointing inbound). In-plane streamlines colored by velocity magnitude

4 Conclusions

The aerodynamic properties of a biomimetic wing have been investigated. The wing design follows an example from nature, the white stork, which shows an excellent performance in soaring flight. Its wing features a cascade of primary feathers on its tip. By performing Navier-Stokes flow simulations of the flow around the re-engineered wing, flow features and aerodynamic properties have been identified. The aerodynamic performance of the wing is close to values observed in and derived from measurements in nature by tracking free flying birds (Eder et al. 2015).

The simulations comprise both RANS and scale-resolving DDES. This allows for an efficient investigation of a wide range of angles of attack as well as getting detailed insight in one selected flight condition. The glide efficiency as well as the sink rate from the measurement are slightly better than the values predicted from a series of RANS calculations. These deviations are accounted to uncertainties in details of the geometric design. Future work will focus on further optimization of the cascade and wing geometry in order to achieve an even better performance. Nevertheless, the results are close to the experimental findings and provide a good quantitative prediction of efficient flying states.

The analysis of flow field results has helped to obtain a closer view to the flow field across the feather cascade. The simulation reveals how the flow from the lower side passes between the primary feathers and generates additional lift before forming a vortex, which is shifted inbound but also far weaker compared to a single-element wing tip. Another counter-rotating inner vortex also has been identified. The impact of these two vortices on the surface flow becomes obvious in surface streamlines. Further outwards, the cascaded configuration produces several weaker tip vortices in spite of the single tip vortex one would expect from a single-element wing tip.

Finally, a strong time-dependence of the aerodynamic forces has been observed in the results from DDES. This behavior appears undesirable and unrealistic for an actual bird. Its occurrence is supposed to be connected with simplifications and neglects in comparison with the real bird, where effects like feather surface structure, permeability and probably a certain amount of elasticity and shape adaptation are counteracting these unsteady effects. Several of these points will be taken up within future work in order to develop models which account for these phenomena and allow for an even deeper understanding of relevant effects for avian flight as well as their technical adaptation.

Author contributions All authors contributed to the study conception and design. Preparation, data collection and analysis were performed by GE and ET. The first draft of the manuscript was written by ET and all authors commented on previous versions of the manuscript. All authors read and approved the final manuscript.

Declarations

Conflict of interest The authors have no Conflict of interest to declare that are relevant to the content of this article.

References

Berens, M.: Potential of multi-winglet systems to improve aircraft performance. PhD thesis, Technische Universität Berlin, Berlin, Germany (2008)

Eder, H., Fiedler, W., Pascoe, X.: Air-permeable hole-pattern and nose-droop control improve aerodynamic performance of primary feathers. J. Comp. Physiol. A. **197**(1), 109–117 (2011). https://doi.org/10.1007/s00359-010-0592-7

Eder, H., Fiedler, W., Neuhäuser, M.: Evaluation of aerodynamic parameters from infrared laser tracking of free-gliding white storks. J. Ornithol. **156**(3), 667–677 (2015). https://doi.org/10.1007/s10336-015-1176-7

FLZ_Vortex. https://flz-vortex.de/flz_vortex.html. Accessed: 2022-07-01

Graham, R.R.: Safety devices in wings of birds. J. R. Aeronaut. Soc. **36**(253), 24–58 (1932). https://doi.org/10.1017/s0368393100111708

Herzog, K.: Anatomie und Flugbiologie der Vögel. G. Fischer, Stuttgart (1968)

KleinHeerenbrink, M., Johansson, L.C., Hedenström, A.: Multi-cored vortices support function of slotted wing tips of birds in gliding and flapping flight. J. R. Soc. Interface **14**(130), 20170099 (2017). https://doi.org/10.1098/rsif.2017.0099

Langtry, R.B., Menter, F.R.: Correlation-based transition modeling for unstructured parallelized computational fluid dynamics codes. AIAA J. **47**(12), 2894–2906 (2009). https://doi.org/10.2514/1.42362

Menter, F.R.: Two-equation eddy-viscosity turbulence models for engineering applications. AIAA J. **32**(8), 1598–1605 (1994). https://doi.org/10.2514/3.12149

Newman, B.G.: Soaring and gliding flight of the black vulture. J. Exp. Biol. **35**(2), 280–285 (1958). https://doi.org/10.1242/jeb.35.2.280

Pascoe, X.: Nachlaufvermessung eines Storchenflügels. Project thesis, Institut für aerodynamik der TU München (2009)

Pennycuick, C.J., Obrecht, H.H., Fuller, M.R.: Empirical estimates of body drag of large waterfowl and raptors. J. Exp. Biol. **135**(1), 253–264 (1988). https://doi.org/10.1242/jeb.135.1.253

Smirnov, P.E., Menter, F.R.: Sensitization of the SST turbulence model to rotation and curvature by applying the spalart–shur correction term. J. Turbomach. **131**(4) (2009). https://doi.org/10.1115/1.3070573

Spalart, P.R., Deck, S., Shur, M.L., Squires, K.D., Strelets, M.K., Travin, A.: A new version of detached-eddy simulation, resistant to ambiguous grid densities. Theoret. Comput. Fluid Dyn. **20**(3), 181–195 (2006). https://doi.org/10.1007/s00162-006-0015-0

Tangermann, E., Klein, M.: Numerical simulation of a separating laminar boundary layer exposed to ambient turbulence. In: 14th WCCM-ECCOMAS congress. CIMNE, Barcelona (2021). https://doi.org/10.23967/wccm-eccomas.2020.238

Tucker, V.A.: Gliding birds: reduction of induced drag by wing tip slots between the primary feathers. J. Exp. Biol. **180**(1), 285–310 (1993). https://doi.org/10.1242/jeb.180.1.285

Tucker, V.A.: Drag reduction by wing tip slots in a gliding harris' hawk, parabuteo unicinctus. J. Exp. Biol. **198**(3), 775–781 (1995). https://doi.org/10.1242/jeb.198.3.775

Weller, H.G., Tabor, G., Jasak, H., Fureby, C.: A tensorial approach to computational continuum mechanics using object-oriented techniques. Comput. Phys. **12**(6), 620 (1998). https://doi.org/10.1063/1.168744